Short Papers

An Efficient Analysis Method for Nonlinear Effects in High-Power HTSC Planar Microwave Circuits

Hongzhen Z. Tang, Safieddin Safavi-Naeini, and Y. L. Chow

***Abstract*—An efficient nonlinear modeling approach, based on combining the method of moment (MoM) with the harmonic-balance (HB) technique, is proposed for the analysis of nonlinear effects of high temperature superconductive microwave planar circuits. The formulation consists of linear and nonlinear analyses. The linear analysis is carried out by using the MoM and adopting complex image Green's function, and the nonlinear analysis is performed by using the HB technique.**

***Index Terms*—Harmonic balance, HTSC nonlinearity, method of moment, nonlinear analysis, superconductor.**

I. INTRODUCTION

Thus far, the applications of high-temperature superconductive (HTSC) microwave circuits are limited to low power level and mainly receiving circuits. In the transmitting mode, when the power level is moderately high, the surface resistance increases moderately, but becomes *nonlinear*. A further increase in power results in a significant increase of the surface resistance. Consequently, the HTSC circuits become very lossy and are even worse than those constructed from conventional conductors. Once the current density exceeds the HTSC material critical current density, the superconductivity disappears and the circuit fails. For some applications, such as the transmitters in communication systems, we have to push the input power level high enough to meet practical requirements.

Experimental studies for HTSC material have been conducted [1]. It has been observed that the dependency of the surface resistance R_s on microwave-frequency magnetic field $H_{\rm rf}$ is well approximated by a quadratic relation as follows:

$$R_s = R_{s0} + R_{s2} H_{\rm rf}^2 \tag{1}$$

where R_{s0} and R_{s2} are constants, and are obtained from measurements. Thus, the nonlinearity of HTSC material can be modeled as a global $v - i$ curve derived from (1) in the form of a power series.

In this paper, a novel method based on the combination of the method of moments (MoM) and the harmonic-balance (HB) technique is proposed and applied to the analysis of the nonlinear behaviors of HTSC thin-film planar microwave integrated circuits. In this method, the field interaction and fringing field outside the HTSC material are included in the MoM formulation by using the complex-image Green's function [2]. Over the HTSC surface, the above-mentioned power series model is used to characterize the nonlinearity of HTSC material. The nonlinear analysis is then carried out by the HB technique. The method has successfully been applied previously to the analysis of an HTSC stripline antenna [3]. Basically, the proposed method is an integral-equation approach. To date, and to our knowledge, there is no fast convergent integral equation method that can be used to analyze the nonlinear HTSC microwave circuits.

The proposed method is explained in Section II. In Section III, an HTSC thin-film end-coupled stripline bandpass filter is studied first. The results obtained are compared with some published measured results to verify the nonlinear modeling. A microstrip line is then investigated for the effects of HTSC nonlinearity on the current distribution and conductor loss. Conclusions are given in Section IV.

II. COMBINED MOM–HB METHOD

The impedance boundary condition on the surface of the HTSC thin-film planar circuit (conducting material) illuminated by an incident wave with electric field $\boldsymbol{E}^{\rm inc}$ is

$$\boldsymbol{n} \times (\boldsymbol{E}^{\rm inc} + \boldsymbol{E}^{\rm sca}) = Z_s \boldsymbol{n} \times \boldsymbol{J}_s \tag{2}$$

where $\boldsymbol{E}^{\rm sca}$ is the scattered electric field, $\boldsymbol{J}_s$ is the surface current density induced on the conductor surface, $Z_s = R_s + jX_s$ is the surface impedance of the conducting material, and $\boldsymbol{n}$ is the outwards unit normal vector. For HTSC materials, the surface impedance Z_s is no longer a constant, but depends on the surface current density $\boldsymbol{J}_s$. Thus, generally speaking, (2) is a nonlinear equation. Thus, this leads to the generation of new harmonically related frequencies. Characterization of a nonlinear material must be done by a time-domain model. In this paper, only the nonlinear effect due to R_s is considered. The nonlinear effect of X_s is small as compared with the total linear field effect, therefore, it is neglected.

Equation (2) is actually an equation of the following general operator form:

$$V_i + L(J_s) = NL(J_s) \tag{3}$$

where V_i represents the applied source voltage, L represents a *linear* operator, in which the *total field* interaction outside and on the structure at the fundamental and harmonic frequencies is taken into account by standard linear field analysis technique, and NL represents a *nonlinear* operator characterizing the property of a nonlinear material. Thus, (3) is the HB equation, in which the total voltages generated by the linear part (including the source) should match the total voltages generated by the nonlinear part at each harmonic frequency.

The linear operator in (3) can then be presented in a matrix form by the MoM formulation, i.e., the linear voltage is as follows:

$$V_L = [V_i] - [Z][I] \tag{4}$$

where $[Z]$ is a *linear* impedance matrix characterizing the field interaction in the surrounding media of the conducting object, $[I]$ represents the currents flowing on the surface of each segment, and $[V_i]$ represents the applied source voltages. All above quantities must be known at each harmonic frequency. The nonlinear operator in (3) must be dealt with in the time domain. Based on (1), the nonlinear characteristic of the material is usually modeled by their global $v - i$ curve as follows:

$$v_{NL} = a_1 i + a_3 i^3 \tag{5}$$

Manuscript received February 15, 2000. This work was supported by Com Dev and the Canadian Space Agency under a Natural Sciences and Engineering Research Council of Canada Collaborative Research Grant.

H. Z. Tang and S. Safavi-Naeini are with the Electrical and Computer Engineering Department, University of Waterloo, Waterloo N2L 3G1, Ont., Canada (e-mail: hztang@aftab.uwaterloo.ca; safavi@maxwell.uwaterloo.ca).

Y. L. Chow is with the Electrical Engineering Department, City University of Hong Kong, Hong Kong. (e-mail: eeylchow@cityu.edu.hk).

Publisher Item Identifier S 0018-9480(00)05549-6.

where the coefficients a_1 and a_3 are dependent on the geometry of the circuit structure and the coefficients in (1) for HTSC material. Equation (5) is in the time domain, whereas (4) is in the frequency domain. Time-to-frequency conversion is achieved using the Fourier transformation (FT). Since excitations are sinusoidal signals and the nonlinear $v - i$ curve is a polynomial, the Fourier series expansion coefficients can be found very easily. The quantities in the frequency domain are simply the coefficients in the Fourier series. On the other hand, the time-domain quantities can be found by taking the sum of amplitudes at each harmonic frequency.

A system of HB equations can be obtained by matching the linear voltage in (4) with the nonlinear voltage in (5) at each harmonic frequency. Thus, the equation for the kth harmonic frequency component is as follows:

$$[V_{i,\,k}] - [Z_k][I_k] = [V_k]. \tag{6}$$

To solve the system of equations (6) for the unknown current in the frequency domain, i.e., I_k, we adopt an iterative procedure. For this purpose, (6) is converted into an iterative form for the unknown current I_k

$$[I_k]^{(p+1)} = [Z_k]^{-1}\left([V_{i,\,k}] - [V_k]^{(p)}\right) \tag{7}$$

where $(*)^{-1}$ represents the inverse of the matrix. The procedure starts from the harmonic current amplitudes $I^{(p)}$ at the pth iteration. We then find its time-domain representation $i(t)$, by taking a finite sum of harmonic terms. Using the time-domain nonlinear equation (5), we can find the voltage $v(t)$ in the time domain. Performing the harmonic expansion of the voltage, we can obtain the voltage V at each harmonic frequency. Equation (7) is then used to obtain the current at the $(p+1)$th iteration in the frequency domain. The procedure is repeated until the following convergent criterion is satisfied for each harmonic:

$$\text{Error} = \frac{\sum_{m=1}^{N} |I_m^{(p)} - I_m^{(p+1)}|^2}{\sum_{m=1}^{N} |I_m^{(p)}|^2} < \text{eps} \tag{8}$$

where eps is a predesignated threshold for error, say, 10^{-6}.

Once the current at different harmonic frequencies is obtained from the above analysis on each segment over an HTSC microstrip line, the effective series resistance and the conductor loss as a function of input power can be determined.

III. NUMERICAL RESULTS AND DISCUSSIONS

In regard to implementation, two important issues should be discussed. One is the initial guess that is very critical for convergence in the HB technique, especially for the microstrip-line circuit because of the edge condition of the current density distribution over the cross section of a transmission line [4]. In the implementation of the nonlinear simulator, the material is first assumed to be linear and the current density distribution is found. This current density distribution is then taken as the initial guess of the current value. This results in very fast convergence. The other is the number of harmonics that has to be included in the simulation in order to obtain reasonable accuracy and, in the meantime, achieve fast computation. In [3], we have tested the frequencies up to the ninth harmonics. For weak nonlinearity, results are indistinguishable with those by only considering the third and fifth harmonics. Since the voltage in (5) is determined only by the odd terms of the current, it is safe to ignore all even harmonics. Therefore, only the third and fifth harmonics are included in this simulation.

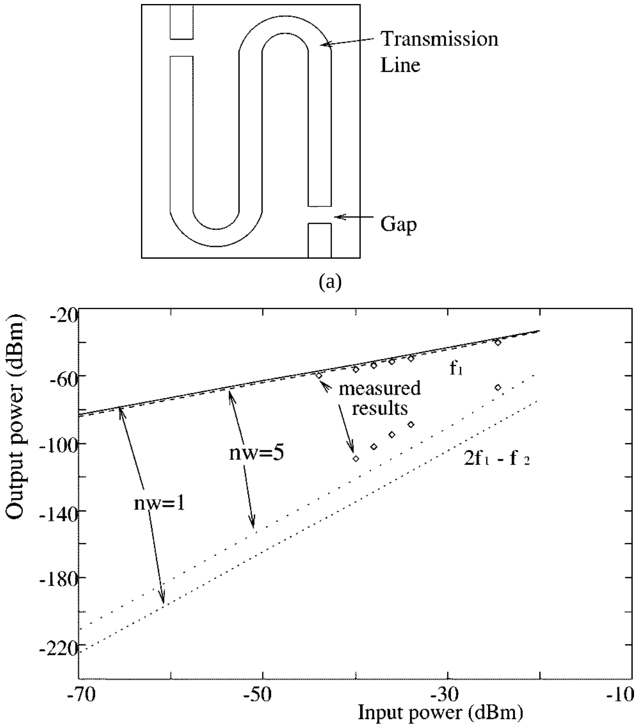

(a)

(b)

Fig. 1. Two-tone intermodulation results of a stripline filter from the simulation and measurement. ("nw" is the number of MoM segments along the transverse direction of the stripline.)

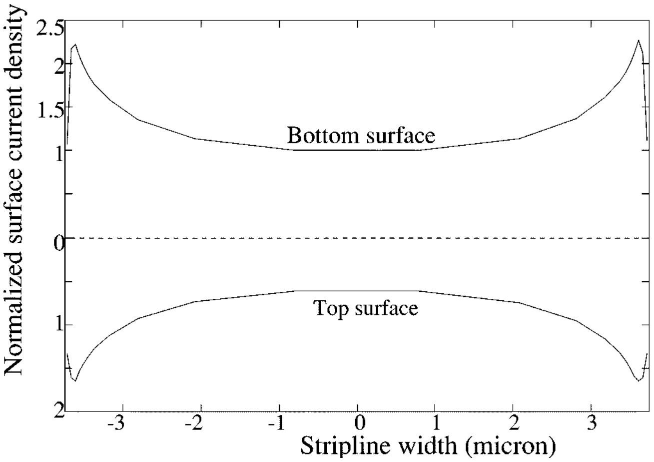

Fig. 2. Surface current density distributions normalized to the center of the bottom surface on the bottom and top surfaces of a finite-thickness HTSC microstrip line at 5-dBm applied power.

To verify the nonlinear modeling method presented here, the stripline filter explained in [1], as shown in Fig. 1(a), is investigated. For a two-tone intermodulation analysis, we compute the output power at the third-order frequency $2f_1 - f_2$, where f_1 is chosen as 1.5 GHz, $f_2 = f_1 + \delta f$, and $\delta f = 1$ kHz. The two signals have same input power. The length of the line is chosen to be a half-wavelength long at the fundamental frequency. The width of the stripline is 150 μm, and the substrate has a thickness of 0.5 mm with $\epsilon_r = 25$. The coefficients in (1) for the nonlinearity of the HTSC material are found by curve

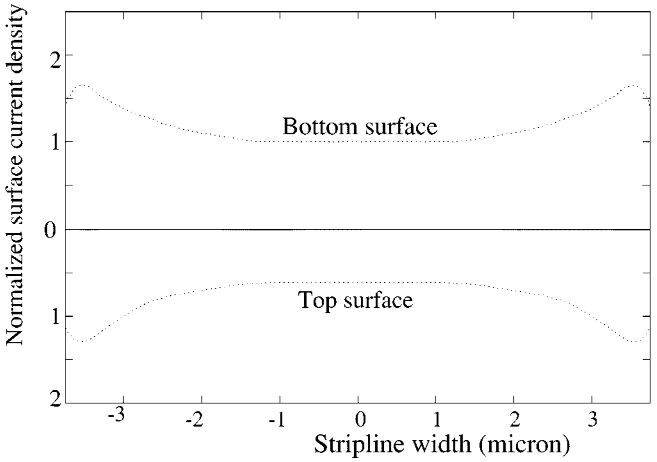

Fig. 3. Surface current density distributions normalized to the center of the bottom surface on the bottom and top surfaces of a finite-thickness HTSC microstrip line from [5].

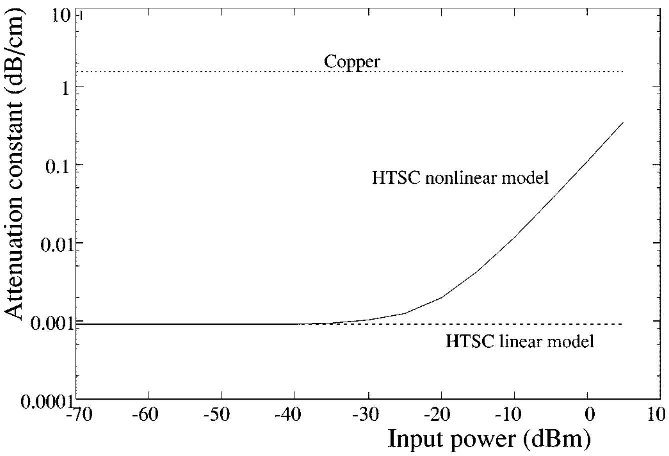

Fig. 4. Attenuation constant versus input power of an HTSC microstrip line at $f = 10$ GHz.

fitting to the measured data given in the same paper, and are given as follows:

$$R_{s0} = 1.4868 \times 10^{-5}\Omega \quad R_{s2} = 4.8270 \times 10^{-9}\Omega/Oe^2. \tag{9}$$

Fig. 1(b) gives the simulation results for output powers at the fundamental frequency f_1 and the third-order intermodulation frequency $2f_1 - f_2$ as a function of input power at the fundamental frequency f_1, together with the measurement results from [1]. From Fig. 1(b), the third-order intermodulation output power obtained with five charge cells along the transverse direction of the stripline is 10 dB higher than those with only one charge cell and much closer to the measurement intermodulation results as well. The measured intermodulation is still about 10 dB larger than that of the five charge-cell case. That gives a numerical error of 5%. The remaining discrepancy is probably due to inaccuracy of the local relation between the surface resistance and the current density obtained from (1) at some segments. The simulation accuracy may be improved by using a more accurate local surface resistance relation and more segments in the transverse direction of the stripline.

Next, an HTSC microstrip line is investigated. The strip has a width of $w = 7.5$ μm, a thickness of $t = 1$ μm, and a length of $L = 6$ mm. When $T = 77$ K, the penetration depth is 0.323 μm. The substrate thickness h is 10 μm with the relative dielectric constant of 13. The frequency is 10 GHz. The coefficients of the power series in (1) are also given in (9). When the applied power is small, there are high current density peaks at the edges, as expected. However, when the applied power is increased, the peaks of the current density distribution shift away from the edges toward the central part of the HTSC strip, as shown in Fig. 2, for the applied power of 5 dBm. Shown in Fig. 3 is another numerical results for the current distribution from [5] for a similar microstrip line obtained by a two-dimensional (2-D) model and finite-difference time-domain (FDTD) approach in conjunction with Ginzburg–Landau (GL) theory. Comparing the results in Fig. 2 with those in Fig. 3, we observe that the general trend for the current distribution over the stripline width as predicted by the two approaches is very close. However, the difference between these two approaches is that the proposed method is the integral-equation approach, which is substantially faster than a differential-equation (i.e., FDTD) approach.

The conductor loss of the HTSC microstrip line as a function of input powers at the operating frequency of 10 GHz is shown in Fig. 4, in which the results from the linear model and for a normal conductor, i.e., copper, are also presented. Below the power level of -35 dBm, the attenuation constant not only is very small, but stays constant as well. However, when the input power is increased, the attenuation starts to increase very rapidly. The linear model fails to predict the conductor loss of the HTSC beyond the -35-dBm power level. The conductor loss for the normal conductor, i.e., copper, remains constant no matter how high the applied power is.

IV. CONCLUSIONS

The combined MoM–HB method for nonlinear modeling of microwave thin-film HTSC circuits has been presented in this paper. The approach was verified through the simulation of the two-tone intermodulation of an HTSC stripline filter. The current density distribution and the conductor loss of an HTSC microstrip line were then studied. The method proposed here is an integral-equation approach, which is substantially faster than a differential equation FDTD-based approach. In addition, the method taking advantage of the basic features of the MoM and the HB technique is efficient, accurate, and suitable for strong nonlinearities.

REFERENCES

[1] D.E. Oates, A. C. Anderson, D. M. Sheen, and A. M. Ali, "Stripline resonator measurements of Z_s versus H_{rf} in $YBa_2Cu_3O_{7-x}$ thin films," *IEEE Trans. Microwave Theory Tech.*, vol. 39, pp. 1522–1529, Sept. 1991.

[2] Y. L. Chow, J. J. Yang, D. J. Fang, and G. E. Howard, "A closed form spatial Green's function for the thick microstrip substrate," *IEEE Trans. Microwave Theory Tech.*, vol. 39, pp. 588–592, Mar. 1991.

[3] S. Safavi-Naeini, H. Z. Tang, and Y. L. Chow, "A fast nonlinear method for the harmonic effects analysis of a HTS stripline structure," in *IEEE AP-S Int. Symp. Dig.*, 1997, pp. 332–335.

[4] S. Safavi-Naeini, R. Faraji-Dana, and Y. L. Chow, "Studies of edge current densities in regular and superconducting microstrip lines of finite thickness," *Proc. Inst. Elect. Eng.*, pt. H, vol. 140, pp. 361–366, Oct. 1993.

[5] A. Mohamed and S. El-Ghazaly, "Nonlinear analysis of microwave superconductor devices using full-wave electromagnetic model," *IEEE Trans. Microwave Theory Tech.*, vol. 43, pp. 2590–2599, Nov. 1995.

Cryogenic Indium–Phosphide HEMT Low-Noise Amplifiers at V-Band

J. M. Tanskanen, P. Kangaslahti, H. Ahtola, P. Jukkala, T. Karttaavi,
M. Lahdes, J. Varis, and J. Tuovinen

Abstract*—Indium–phosphide (InP) high electron-mobility transistors potentially have the lowest noise at frequencies below 100 GHz, especially when cryogenically cooled. We have designed monolithically integrated InP millimeter-wave low-noise amplifiers (LNA's) for the European Space Agency (ESA) science Planck mission. The Planck LNA's design goal for noise temperature is 35 K at the ambient temperature of 20 K. The operation bandwidth is over 20% at 70 GHz. The maximum allowable power consumption for a Planck LNA (gain 20 dB) is $P_{\rm dc} = 5$ mW at 20 K. The chosen foundry for these LNA's was DaimlerChrysler Research, Ulm, Germany. The DaimlerChrysler 0.18-μm InP process was used. This process is well suited for V-band LNA design, giving sufficient gain with very low noise. Several one-, two-, and three-stage amplifiers were designed. The best of them exhibited a noise figure lower than 5.5 dB with a gain higher than 14 dB over the 50–68-GHz range at room temperature. The best single-stage amplifier demonstrated a noise figure of 4.5 dB and a gain higher than 5 dB from 50 to 60 GHz at room temperature. On-wafer measurements on these monolithic-microwave integrated circuits (MMIC's) have been done at MilliLab, Espoo, Finland. For the module fabrication, MMIC chips will be mounted in a WR-15 waveguide split-block housing.

***Index Terms*—Cryogenic cooling, indium–phosphide, LNA, V-band.**

I. INTRODUCTION

The Planck mission[1] includes a high-frequency instrument (HFI) and a low-frequency instrument (LFI). The LFI[2] [3] receivers at 30, 44, 70, and 100 GHz will form an array of 56 sensors. This work has been performed as part of the technology evaluation program for the Planck LFI front-end instruments. Thus far, we have designed 60- and 70-GHz low-noise amplifiers (LNA's) using the DaimlerChrysler 0.18-μm InP high electron-mobility transistor (HEMT) process.

The designed circuits were simulated to have 3–4-dB noise figure at room temperature. A reduction by a factor of 6–8 in the noise temperature is typically expected at cryogenic temperatures corresponding to a physical temperature of 20 K.

II. MODELING AND DESIGN OF THE LNA'S

As the DaimlerChrysler process was under further development and devices were not yet fully characterized by the foundry, we performed measurements to model the transistors. This was done at MilliLab, Espoo, Finland, using a sample wafer from a previous run. Due to time limitations, effort was concentrated on a 2 × 40 μm device model, as suggested by the foundry. Optimum bias conditions for minimum noise were derived. The optimum noise measure M was found to be at $V_{\rm ds} = 1$ V and $I_{\rm ds} = 10$ mA. The contour plot for noise measure M was done using contour plots ranging $V_{\rm ds}$ from 0 to 3 V and $I_{\rm ds}$ from 0 to 30 mA. Noise parameters for modeling were measured at room temperature from 60 up to 74 GHz [1]. The optimum bias point for minimum noise figure was selected by measuring not only M, but also noise parameters at several bias points. The noise parameters were used to verify the M measurements. The minimum noise figure $F_{\rm min}$ was 2.4 dB, noise resistance R_n was 7 Ω, and optimum noise impedance $\Gamma_{\rm opt}$ was (0.37 $\angle$ 175°) at 64 GHz. MilliLab derived a small-signal model with noise for simulations [2]. It uses simple circuit theory arguments to show that, for an intrinsic device, two frequency-independent constants of the intrinsic gate resistance and drain resistance need to be known. In order to predict all four noise parameters, a small-signal model is also needed. The noise sources at the constant resistances (R_s, R_d, and R_g) are at physical temperature T_a of the device, while the gate and drain are at the equivalent noise temperatures T_g and T_d, respectively. It was shown in [2] that T_g is equal to T_a at room and cryogenic temperatures. The noise constant T_d is used to fit the model to the measurements. Fig. 1 shows the small-signal noise model for 2 × 40 μm HEMT.

The LNA's were designed using coplanar waveguides (CPW's). CPW's have not been modeled as thoroughly as microstrip lines, but recently they have been a subject of increasing interest in research [3]. The foundry provided us models of the most common structures, such as transmission lines, cross junctions, and T-junctions. At this stage, the choice of different structures was still rather limited, which imposed some restrictions concerning the layout. For instance, line impedances were limited to 34, 50, and 67 Ω. Air bridges were used across the lines, where discontinuities existed. This suppresses the even mode and connects all the grounded regions together. The use of air bridges increases the cutoff frequency of the slotline modes, leading to a successful single-mode operation.

III. MEASURED LNA PERFORMANCE AT ROOM AND AT CRYOGENIC TEMPERATURES

LNA's were measured first at room temperature and then cooled down to cryogenic temperatures. Measured and simulated S-parameters and the noise figure for a three-stage LNA are shown in Figs. 2 and 3. The minimum noise figure at the V-band was 4.6 dB, which corresponds to 546-K noise temperature. Noise was measured in [4] at room temperature at the W-band in the range of 250–470 K. This indicates that further improvement in the noise temperature is still needed.

With cooling, mobility of the electrons increases around 3.5 times and scattering of the electrons is reduced. These phenomena make transconductance g_m higher. It increases from 30% to 75% depending on device and bias point [5]. In [6] and [7], the authors suggest a 0.01–0.02-dB/K gain increase rate. We measured a 0.05-dB/K increase in gain for a single-stage LNA and 0.08 dB/K for a three-stage LNA at 70 GHz. Gain increase is not due to increased bias current because the bias current was kept constant by tuning. The main gain increase was measured within the cooling range from 300 to 100 K. After that, only minor changes were observed.

IV. CONCLUSION

Several InP cryogenic monolithic-microwave integrated-circuit (MMIC) LNA's were designed, processed, and measured. The highlights are as follows. The best single-stage amplifier demonstrated a noise figure of 4.5 dB and a gain higher than 5 dB from 50 to

Manuscript received March 10, 2000. This work was supported by the European Space Agency under ESA Contract 12 851/98/NL/NB.

J. M. Tanskanen, P. Kangaslahti, H. Ahtola, and P. Jukkala are with YLINEN Electronics Ltd., FIN-02700 Kauniainen, Finland (e-mail: juha.tanskanen@ylinen.fi).

T. Karttaavi, M. Lahdes, J. Varis, and J. Tuovinen are with MilliLab, VTT Information Technology, Espoo, Finland (e-mail: timo.karttaavi@vtt.fi).

Publisher Item Identifier S 0018-9480(00)05553-8.

---

[1] [Online]. Available HTTP: http://astro.estec.esa.nl/Planck/

[2] [Online]. Available HTTP: http://astro.estec.esa.nl/SA-general/Projects/Planck/lfi/lfi_top.html

[3] [Online]. Available HTTP: http://astro.estec.esa.nl/Planck/technical/payl/node6.html

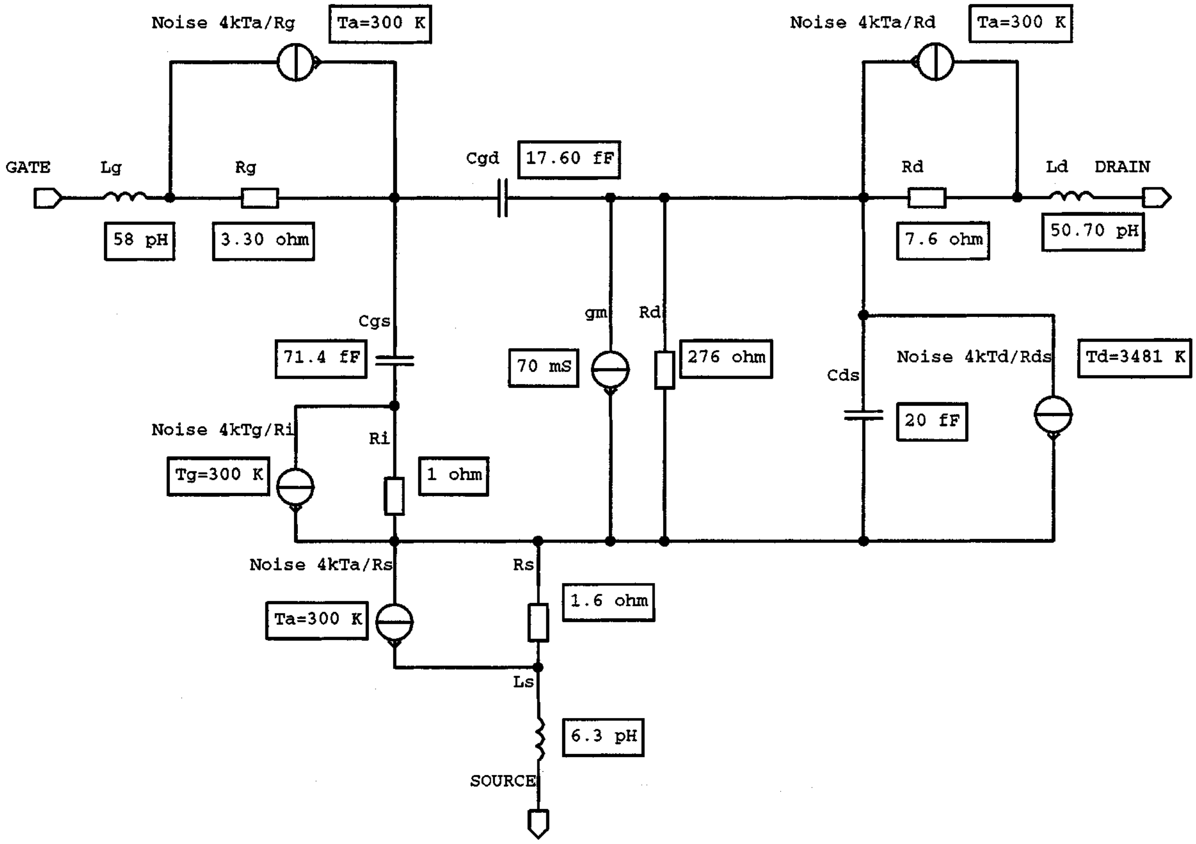

Fig. 1. Small-signal model with noise for 2 × 40μm InP HEMT [2].

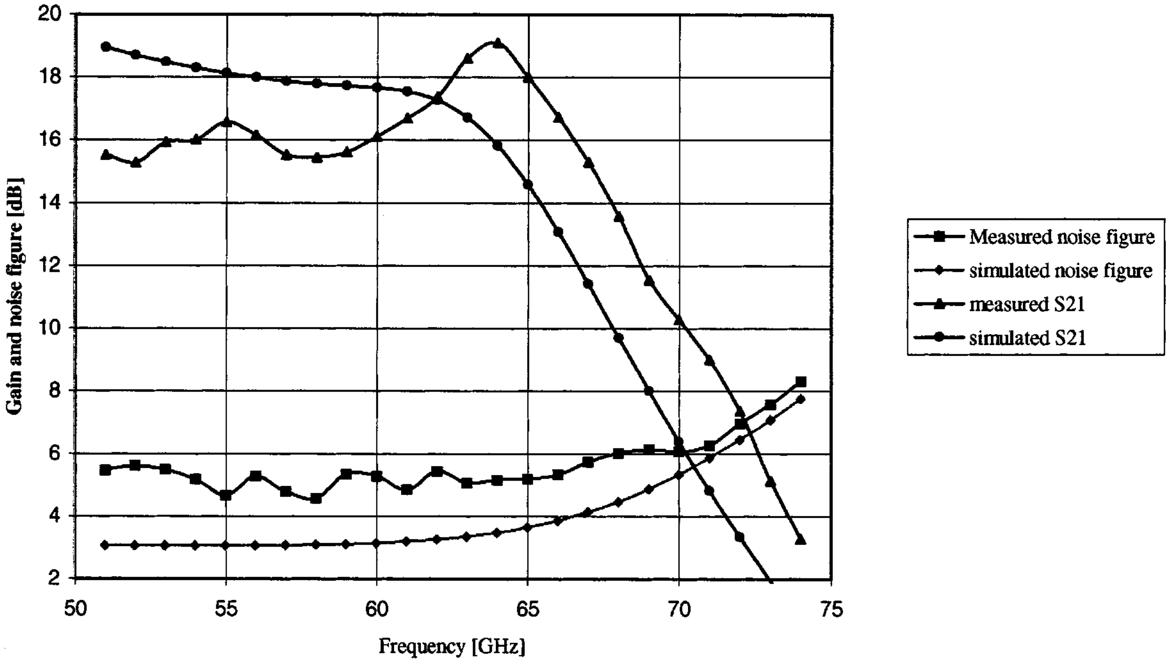

Fig. 2. Measured and simulated gain and noise figure for a three-stage InP LNA at room temperature.

60 GHz (see Fig. 4). The best three-stage LNA exhibited a noise figure lower than 5.5 dB with a gain higher than 14 dB over a 50–68 GHz frequency range. Layout for the three-stage LNA is shown in Fig. 5. Measured noise figure was 2–3 dB higher than

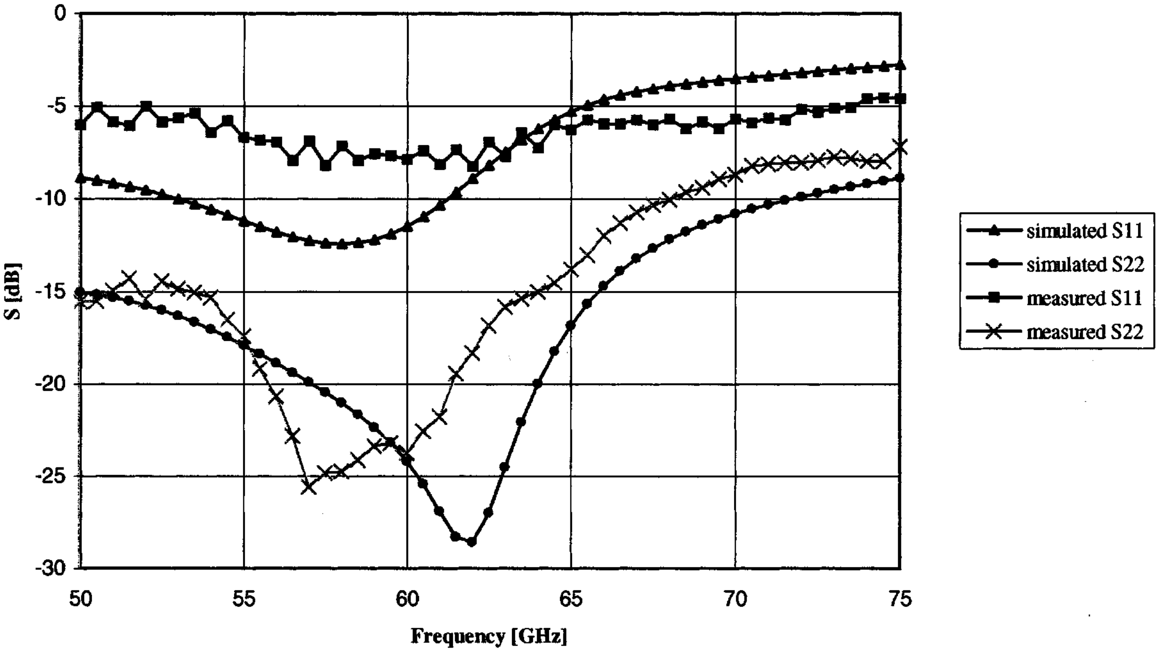

Fig. 3. Measured and simulated S_{11} and S_{22} for a three-stage InP LNA at room temperature.

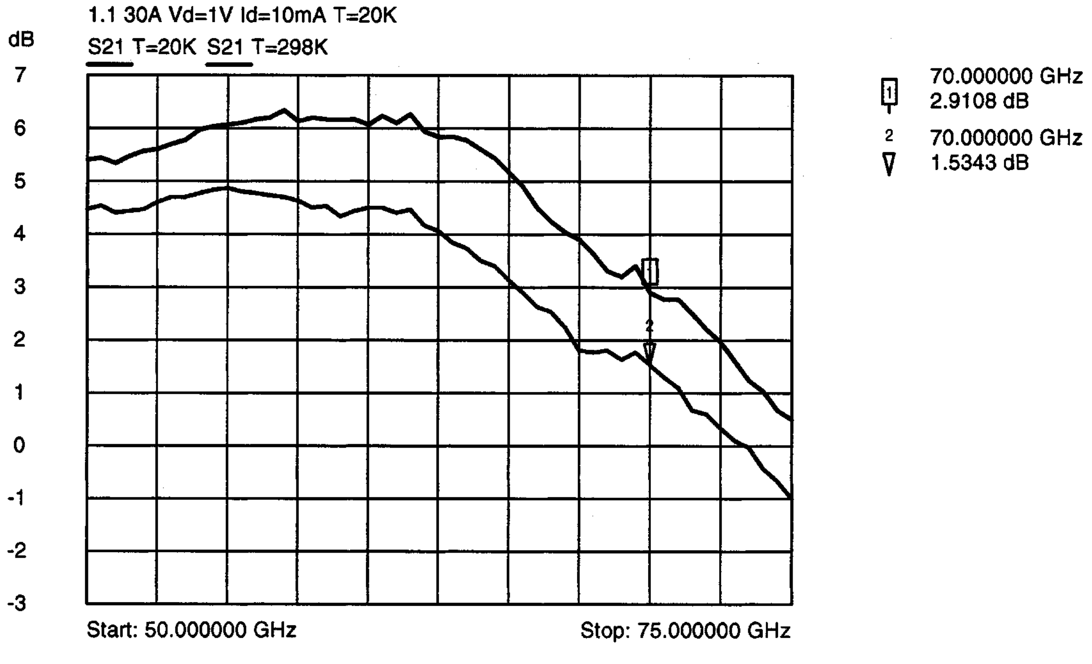

Fig. 4. Measured on-wafer S_{21} for a one-stage InP LNA at room temperature and 20 K.

simulated. Simulation model was based on the provided test-wafer measurements. On-wafter measurement setup is shown in Fig. 6. Minimum noise figure of the test transistors on the test wafer was 0.5–1 dB lower than that in the processed wafer. In the test wafer, the transconductance of the transistors was 70 mS and, in the processed wafers, was 45 and 54 mS. This explains the difference in the gain and noise figure.

The measured gain increase rate was 0.05–0.08 dB/K, while the LNA were cooled down to 20 K. This is higher than in [6] and [7], and most of the gain increase was observed above 100 K.

The results can be considered promising, but still leave much room for improvement. For future design iterations, we hope to increase the accuracy of the transistor modeling and overcome the layout and device scaling limitations.

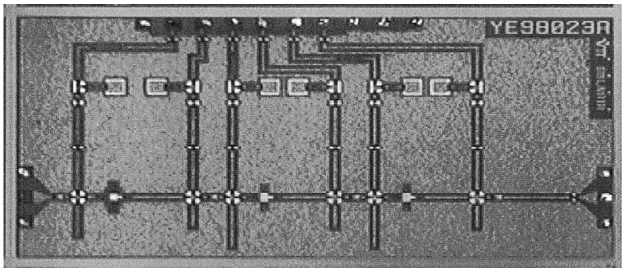

Fig. 5. Layout for three-stage InP LNA. MMIC chip size is 2930 × 1430 μm.

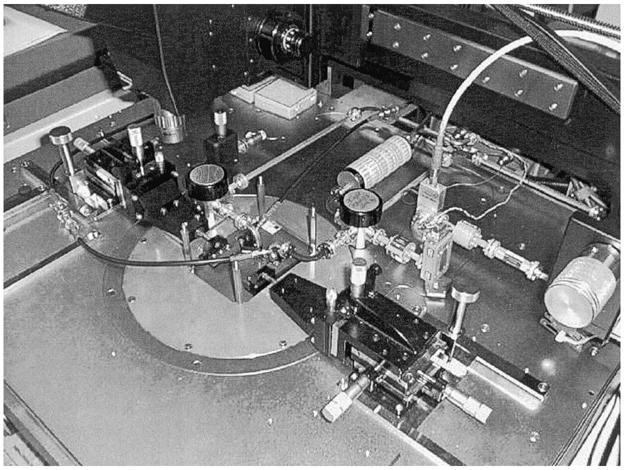

Fig. 6. On-wafer noise parameter measurement setup for V-band.

REFERENCES

[1] M. Lahdes and J. Tuovinen, "V-band on-wafer noise parameter measurements," in *GaAs'98 Dig.*, Amsterdam, The Netherlands, 5–6, pp. 39–44.

[2] M. W. Pospieszalski, "Modeling of noise parameters of MESFET's and MODFET's and their frequency and temperature dependence," *IEEE Trans. Microwave Theory Tech.*, vol. 37, pp. 1340–1350, Sept. 1989.

[3] T. Sporkmann, "The current state of the art in coplanar MMICs," *Microwave J.*, pp. 60–74, Aug. 1998.

[4] S. Weinreb, R. Lai, N. Erickson, T. Gaier, and J. Wielgus, "W-band InP wide-band MMIC LNA with 30-K noise temperature," in *IEEE MTT-S Int. Microwave Symp. Dig.*, 1999, pp. 101–104.

[5] K. H. G. Duh, M. W. Pospieszalski, W. F. Kopp, P. Ho, A. A. Jabra, P. Chao, P. M. Smith, L. F. Lester, J. M. Ballingall, and S. Weinreb, "Ultra-low-noise cryogenic high-electron-mobility transistors," *IEEE Trans. Electron Devices*, vol. 35, pp. 249–256, Mar. 1988.

[6] H. Wang, D. C.-W. Lo, R. Lai, C.-C. Yang, and J. Berenz, "Cryogenically cooled performance of a monolithic 44-GHz InP-based HEMT low-noise amplifier," *IEEE Microwave Guided Wave Lett.*, vol. 5, pp. 281–283, Sept. 1995.

[7] A. Sylvestre, "Cryogenic investigation of gate leakage and RF performances down to 50 K of 0.2 μm AlInAs/GaInAs/InP HEMTs," *Electron. Lett.*, vol. 20, no. 24, pp. 2152–2154, Nov. 1993.

Investigating High-T_c Superconductors—A Cryogenic Microwave Broad-Band Calibration

T. Reuss and J. Richard

***Abstract*—A new cryogenic microwave broad-band calibration method for the measurement of the complex input impedance of a one-port network is presented in this paper. The complex impedance is calculated from measurements of the complex reflection coefficient made by a vector network analyzer. To validate the method, low-temperature measurements of metallic microstrips with a known temperature behavior of the resistivity were compared to simulations. Its broad-band nature makes it particularly powerful when exploring a region of the magnetic-field temperature-frequency parameter space of superconductors that was previously inaccessible with a comparable accuracy.**

***Index Terms*—Conductivity measurement, cryogenics, frequency response, high-temperature superconductors, impedance, microwave measurements, microwave reflectometry, thin films.**

I. INTRODUCTION

Broad-band microwave measurements are a powerful tool for studying the properties of conductors and dielectrics. Especially when trying to investigate the mixed state in type-II superconductors, the measurement of the complex input impedance carried out over a broad range of frequencies, temperatures, and magnetic fields can provide valuable insight into the vortex dynamics.

The information obtained from such measurements are important, both for technological and fundamental reasons. From a technological point-of-view, it is important to characterize the pinning forces and activation barriers preventing dissipating vortex motion in both RF and dc applications. From a more fundamental point-of-view, it can help to understand what laws govern the vortex motion. Can we describe it with a mean-field single-vortex models, as proposed by Coffey and Clem [1]? Or is the vortex motion better described by collective models (see, e.g., Fisher *et al.* [2])?

The most commonly employed techniques use resonant structures. While allowing what are potentially very sensitive surface impedance studies, these techniques are limited to, at most, a few discrete frequencies. This can be a serious drawback when interpreting the experimental data, as the results can often be described by an uninformative or unreliable parametrization of the data.

More broad-band techniques based on waveguides can be used for investigating the frequency dependence of the vortex state [3]. However, these techniques are still limited to the operating frequency range of the waveguide.

Thus far, to the best of our knowledge, only 300-K calibrations, corrected for low-temperature effects, were used, as described by Xavier [4] or Booth *et al.* [5].

In this paper, a secondary open short load (OSL) broad-band calibration method is presented. It is based on a primary OSL calibration performed at 300 K. It allows measurements at arbitrary frequencies in the RF and microwave range, at (almost) arbitrary temperatures. The frequency range presented here is 0.16–20 GHz and the temperature range is 4–300 K. However, it is, in principle, possible to use this calibration at much higher temperatures.

Manuscript received February 23, 2000.

The authors are with the Centre de Recherches sur les Trés Basses Températures, Centre National de la Recherche Scientifique, 38042 Grenoble, France.

Publisher Item Identifier S 0018-9480(00)05555-1.

A network analyzer (HP 8720B) is used to measure the complex reflection coefficient Γ. Standard transmission-line theory and a mismatch model for coaxial connections [6] are used to extract the complex input impedance Z_i of the microstrip.

II. CALIBRATION METHOD

The complex reflection coefficient Γ of a complex sample impedance Z is given by

$$\Gamma = \frac{Z - Z_c}{Z + Z_c} \tag{1}$$

where $Z_c = 50\ \Omega$ is the characteristic impedance of the connecting transmission line.

However, this expression is only valid if the measurement is performed directly at the location of the sample. In practice, the experimentally measured Γ will include a number of imperfections inherent in any real network analyzer system, like the test set, transmission lines, and connectors that are necessary to carry out the measurement. Therefore, a calibration is needed to eliminate the effect of these imperfections, which becomes increasingly important as the frequency rises and the wavelength decreases to less than the system dimensions.

It is conventional to model the imperfect network analyzer, measuring a one-port network, as a perfect network analyzer connected to the one-port network via a two-port embedding network with scattering matrix $\mathbf{S}$.

Knowing $\mathbf{S}$, the sample's true reflection coefficient Γ_s can be calculated from the measured reflection coefficient γ_s by using the bilinear transform

$$\Gamma_s = \frac{\gamma_s - S_{11}}{\gamma_s S_{22} - (S_{11}S_{22} - S_{12}S_{21})}. \tag{2}$$

One possible method of determining $\mathbf{S}$ is an OSL-type calibration that involves measuring three known precision loads: an open-circuit, a short-circuit, and a 50-Ω load, mounted in the location of the sample.

However, the determination of $\mathbf{S}$ can be completely avoided by substituting three admittances $\{y_j\}$ and their corresponding reflection coefficients $\{\gamma_j\}$ into (2) (see Fig. 1). Thus, for a measured total reflection coefficient γ_s, the corresponding admittance y_s is given by

$$y_s = -\frac{\Delta_{s1}\Delta_{32}y_3y_2 + \Delta_{s2}\Delta_{13}y_1y_3 + \Delta_{s3}\Delta_{21}y_2y_1}{\Delta_{s1}\Delta_{32}y_1 + \Delta_{s2}\Delta_{13}y_2 + \Delta_{s3}\Delta_{21}y_3} \tag{3}$$

with $\Delta_{ij} = \gamma_i - \gamma_j$ and $\Delta_{sj} = \gamma_s - \gamma_j$.

In principle, this calculation can be performed with three arbitrary admittances. Nevertheless, as for the OSL calibration, it is advantageous to use admittances close to open/short/50-Ω loads for a better final resolution.

These three low-temperature compliant loads must be made out of the *same* connector used to connect the superconducting samples (see Fig. 1). However, in contrast to a standard OSL calibration, where the Unfortunately, when the sample is at cryogenic temperatures, the temperature dependence of the calibration loads, which have to be low-temperature compliant, becomes a factor. To our knowledge, these specifications are not met by the calibration loads available.

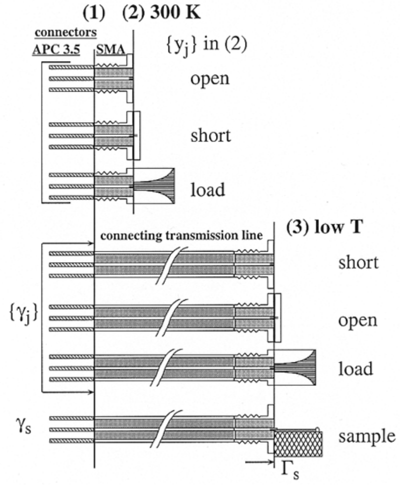

Fig. 1. Sketch of the new calibration method. It consists of six calibration measurements and the sample measurement. After the calibration, the reference plane for the reflection coefficient measurements is in (3) at low temperature.

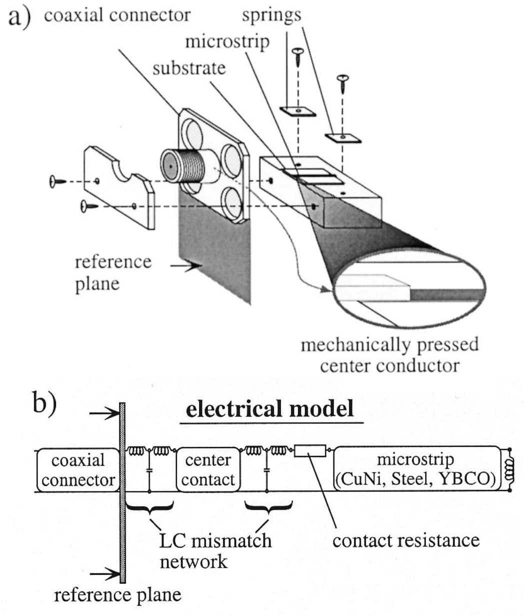

Fig. 2. (a) Experimental setup of the sample. (b) Corresponding electrical model.

knowledge of an electrical model for the loads is crucial, but very difficult to gain, no electrical model for the low-temperature behavior is needed for the new calibration method.

The open and short are made out of standard SMA connectors. The 50-Ω load is commercially available from RADIALL, Rosny Sous Bois, France.

In principle, all six of these measurements $\{y_j, \gamma_j\}$ must be conducted at the same temperature as the sample (e.g., 81 K). Now, as we mentioned earlier, a calibration load actually consists of a connector and the load. The temperature dependence is primarily affected by the connector (a distributed element in the electrical model). Thus, by eliminating the connector right from the beginning of the calibration on, one obtains loads that are temperature independent.

This is done by characterizing the APC3.5/SMA connection using a model proposed by Oldfield [6]. It takes into account the geometrical misfit between the two connection standards. The losses from the

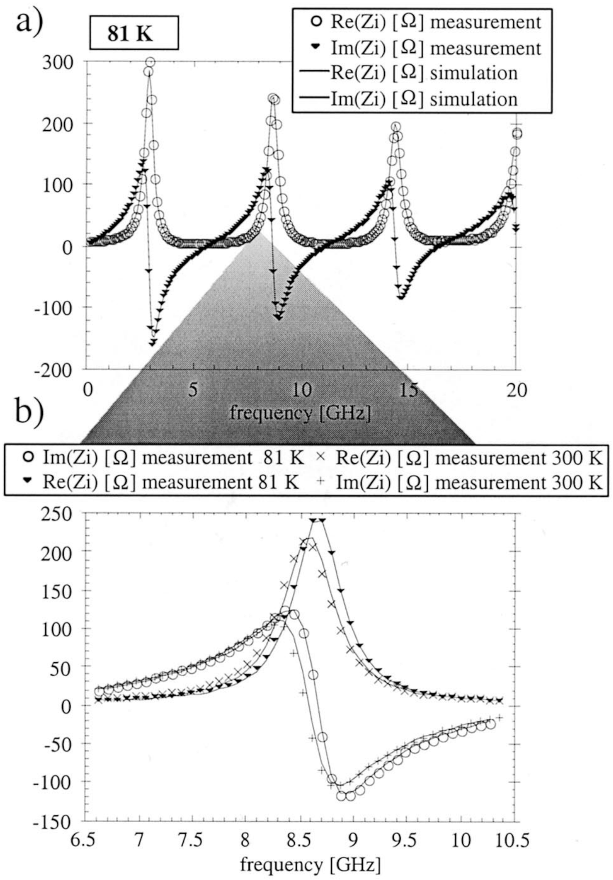

Fig. 3. (a) Input impedance of a copper nickel microstrip using the new calibration method at 81 K and comparison with the simulation obtained with the electrical model indicated in Fig. 2. (b) Zoom on the second resonance, where the room temperature measurement with its simulation is shown for comparison.

gold-plated SMA connector turned out to be much higher than expected. Thus, it was necessary to take into account the resistivity of the underlying bronze beryllium. Using this model to shift the reference plane from (1) to (2) (see Fig. 1), measured—that is to say known—lumped elements $\{y_{co}, y_{cc}\}$ are obtained for which no specific electrical model is needed any more. These admittances $\{y_{co}, y_{cc}\}$ measured at 300 K are identical to the low-temperature values within the measurement accuracy.

In contrast, the 50-Ω load is temperature dependent. It was, therefore, necessary to develop a special device for it where the transmission line is maintained at room temperature. Hence, only the end of the connector is at low temperature and a high-temperature gradient is produced in the connector. This device allows the measurement of the 50-Ω load to be conducted at the same temperature as the sample by simply introducing the device into a Dewar of liquid helium. The temperature can be controlled by varying the depth of the load in the Dewar.

The procedure for this calibration method is as follows (see Fig. 1). First, a primary OSL calibration is performed at room temperature, which places the reference plane in (1). The reference plane is shifted by deembedding from (1) to (2), as mentioned beforehand. The reflection coefficients of the three loads $\{\gamma_j\}$ are then measured under the same experimental conditions as the sample and, finally, the sample (γ_s) itself is measured. Using (3) and (1), we can extract the true reflection coefficient Γ_s of the sample.

III. VALIDATION

Being based on a previously performed OSL calibration, the new method keeps the random and systematic errors of this kind of calibration. The error due to the special high-gradient device was estimated to be less than 2%, by measuring the dielectric permittivity of liquid nitrogen with the open-ended connector.

It appears that the thermal conditions in the connecting cables have to be *identical* for all the low-temperature measurements. It is possible, for instance, to get differences of 240 MHz on the resonance frequency for the same total temperature gradient of 220 K (300–80 K) just by cooling the cryostat differently for the low-temperature measurements.

In order to get an idea of the absolute precision of the new calibration method, we designed and measured samples where the YBa$_2$Cu$_3$O$_{7-\delta}$ microstrip was replaced by resistive metals (copper nickel alloy (CuNi) with $\rho_{300\,\mathrm{K}} = 23\ \mu\Omega \cdot$ cm and stainless steel with $\rho_{300\,\mathrm{K}} = 120\ \mu\Omega \cdot$ cm).[1] The temperature dependence of ρ was measured using a standard four-probe technique.

Fig. 2 shows the experimental setup and corresponding electrical model. The contact resistance was necessary to account for a slight dissymmetry in the low-impedance regime mainly visible with low-resistivity microstrips like gold. Nevertheless, the influence of the contact resistance as well as the high losses in the connector are visible at low temperature.

Fig. 3(a) shows the comparison between the measured and simulated input impedance Z_i of a copper–nickel microstrip at 81 K. The zoom on the second resonance (b) emphasizes on the fact that even the small changes anticipated between high and low temperatures are resolved.

The only parameters that have been changed between the high- and the low-temperature simulation were either measured $(\rho(T))$ or taken from literature (thermal expansion coefficient and dielectric permittivity ε_r [7]–[9]).

The impedance mismatch network was kept constant, which is not really expected because of the differential thermal contractions at the location of the mismatch. Nevertheless, the match is very good.

IV. CONCLUSION

A new calibration method at microwave frequencies has been presented, which allows the simultaneous measurement of the real and imaginary part of the complex input impedance over a broad range of temperatures, frequencies, and magnetic field. Validation experiments on highly resistive metallic microstrips confirm that this method can provide accurate measurements of the complex input impedance in the temperature range of the superconducting transition of high-T_c superconductors.

REFERENCES

[1] J. R. Clem and M. W. Coffey, "Unified theory of effects of vortex pinning and flux creep upon the RF surface impedance of type-II superconductors," *Phys. Rev. Lett.*, vol. 67, no. 3, pp. 386–389, July 1991.

[2] D. S. Fisher, M. P. A. Fisher, and D. A. Huse, "Thermal fluctuations, quenched disorder, phase transitions, and transport in type-II-superconductors," *Phys. Rev. B, Condens. Matter*, vol. 43, no. 1, pp. 130–159, Jan. 1991.

[3] M. Golosovsky, D. Davidov, E. Farber, T. Tsach, and M. Schieber, "Microwave transmission and harmonic generation in granular high-T_c superconducting films: Evidence for flux motion and weak links," *Phys. Rev. B, Condens. Matter*, vol. 43, pp. 10 390–10 398, May 1991.

[4] P. Xavier, "Etude de la response hyperfréquence des vortex dans des couches minces supraconductrices à haute température critique," Ph.D. dissertation, Dept. Phys., Université Joseph Fourier, Grenoble, France, 1994.

---

[1] The (CuNi) sample was patterned by wet etching the stainless-steel sample by Argon ion etching.

[5] J. C. Booth, D. H. Wu, and S. M. Anlage, "A broadband method for the measurement of the surface impedance of thin films at microwave frequencies," *Rev. Sci. Instrum.*, vol. 65, no. 6, pp. 2082–2090, June 1994.
[6] B. Oldfield, "The connector interface and its effect on calibration accuracy," *Microwave J.*, pp. 106–114, Mar. 1996.
[7] B. Yates, R. F. Cooper, and A. F. Pojur, "Thermal expansion at elevated temperatures: II. Aluminum oxide: Experimental data between 100 and 800 K and their analysis," *J. Phys. C, Solid State Phys.*, vol. 5, pp. 1046–1058, 1972.
[8] R. Shelby, J. Fontanella, and C. Andeen, "The low temperature electrical properties of some anisytropic crystals," *J. Phys. Chem. Solids*, vol. 41, pp. 69–74, 1979.
[9] J. Krupka, R. G. Geyer, M. Kuhn, and J. H. Hinken, "Dielectric properties of single crystals of Al_2O_3, $LaAlO_3$, $NdGaO_3$, $SrTiO_3$ and MgO at cryogenic temperatures," *IEEE Trans. Microwave Theory Tech.*, vol. 42, pp. 1886–1890, Oct. 1994.

Space-Based High-Temperature Superconductivity Experiment—Design and Performance

E. Polturak, G. Koren, I. Flohr, R. Waller, and M. Guelman

***Abstract*—In this paper, we describe the first successful superconductivity experiment in space. The experiment aims to test the long-term survivability of high-temperature superconductors (HTS's) under space conditions. Our system consists of a thin $YBa_2Cu_3O_7$ film integrated with a cryocooler. The experiment orbits the earth aboard the TECHSAT II satellite as of July 1998. Periodic testing of the device returns data on its resistance, critical temperature, and critical current. As of now, the superconducting film has shown a marginal degradation of its properties. We hope to provide the basic long-term survivability data needed to advance applications of HTS's in space-based communication systems.**

***Index Terms*—High-temperature superconductivity, satellite communications, superconducting films.**

I. INTRODUCTION

Among the future applications of high-temperature superconductors (HTS's), that of satellite communications seems very promising, both in terms of new technology and economic impact. Given the large demand for communication satellites needed for global coverage providing fast data transmission, it is important to develop more efficient low-loss narrow-band filters needed to minimize interference between communication channels. Another property that is very important in this context is the weight and volume of such devices. HTS's have the potential to realize these goals, provided the technological hurdles can be overcome. These fact were realized early on, and a program to demonstrate operation of HTS components in space was initiated by Nisenoff and coworkers at the Naval Research Laboratory (NRL), Washington, DC, as early as 1988. This program, called the "High Temperature Superconductivity Space Experiment" (HTSSE), was divided into two phases, the first of which, HTSSE-I, was supposed to check the survivability of relatively simple HTS devices in space [1]. This part of the program did not survive the launch. The second phase, HTSSE-II, was designed to test more advanced subsystems and cryocoolers [2]. HTSSE-II was launched into space in February 1999. Thus, the fundamental question, that of long-term survivability of HTS materials in space, remains to be answered. Specifically, one has to check how does the material behave under prolonged exposure to radiation, vacuum, and repeated thermal cycling. Our experiment attempts to answer this question, as well as that relating to the combination of an HTS device with a cryocooler [3].

II. EXPERIMENTAL DETAILS

This experiment was largely defined by limitations imposed by the satellite itself. TECHSAT II is a microsatellite designed and built at the Asher Space Institute, Technion—Israel Institute of Technology, Haifa, Israel, as part of a project developing a low-cost vehicle that can be deployed relatively fast and is, therefore, especially suitable for testing novel space-related technologies [4].[1] It has a shape of a cube, 45 cm on a side, and weighs 48 kg. A significant part of its internal volume is taken by the stabilizing hardware, including a flywheel and three orthogonal electromagnets, which are used to orient the satellite via their interaction with the magnetic field of the earth. By far the largest limitation on the design of on-board experiments comes from the power budget. The satellite is powered by solar cells, which coat four of the six faces of the cube. In order to simplify the design, no external solar panels were used. The fifth face, pointing away from the Earth, is the cold panel. Our experiment is mounted on that panel. The communication antenna, a video camera, and some of the other experiments are mounted on the sixth panel, facing the Earth. Since the surface area covered by the solar panels is small, the total power generated is only 25 W. Approximately 8 W are dedicated to housekeeping, i.e., computer control, telemetry, and stabilizers. This leaves 17 W for all experiments on board, which means that these cannot be operated simultaneously. In fact, the first version of our experiment had to be scrapped because it used a cryocooler that needed 27 W to operate. The cryocooler actually used in this experiment, i.e., the K-508,[2] has a much lower power consumption of only 12 W. The nominal cooling power is 0.5 W at 77 K. The limitations imposed by the power budget dictate that our experiment can be operated only for a short period at a time, typically less than 1 hr. Within that time, the cryocooler must cool the experiment well below T_c. This, in turn, limits the thermal mass of the experiment. The total mass attached to the cold finger was about 5 gm. During the tests in the laboratory, we found that without thermal shielding, the cool-down time was prohibitively long. After adding a single Al shield around the cold finger, the cool-down time decreased down to approximately 15 min.

Our device itself consists of a 300-nm-thick epitaxial c-axis YBCO thin film. The film was grown by laser ablation deposition on a 10×10 mm^2 (100) MgO substrate. We used ion milling to pattern the film into a microbridge, 40-μm wide and 500-μm long. Dry etching was preferred since it is our experience that residues after chemical etching may decrease the lifetime of the device. Au contact pads were also deposited by laser ablation and annealed at 600 °C in an O_2 atmosphere. The finished device had a T_c of 90 K, and a critical current density J_c of 10^6 A/cm^2 at 84 K. A schematic view of the experiment is shown in Fig. 1. The device is glued onto an Al block

---

Manuscript received March 6, 2000. This work was supported by the Israel Science Foundation, by the Heinrich Hertz Minerva Center for High Temperature Superconductors, and by the VPR Fund for Research at Technion—Israel Institute of Technology.

E. Polutrak and G. Koren are with the Physics Department, Technion—Israel Institute of Technology, Haifa 32000, Israel.

I. Flohr, R. Waller, and M. Guelman are with the Asher Space Institute, Technion—Israel Institute of Technology, Haifa 32000, Israel.

Publisher Item Identifier S 0018-9480(00)05556-3.

[1] [Online]. Available: http://techsat.internet-zahav.net/

[2] The K-508 cryocooler is made by RICOR Ltd., Kibbutz Ein-Harod Ihud, Israel.

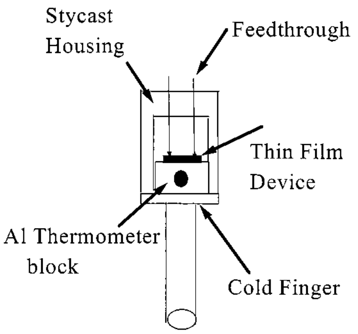

Fig. 1. Schematic view of the cold part of the experiment.

containing a diode thermometer using Ag loaded epoxy. The Al block is then glued to the surface of the cold finger using the same method. A housing machined from 1266 Stycast epoxy surrounding the device and the Al block completes the assembly. The housing is attached to the cold finger using four screws, of size 0–80 in. Electrical connections to the device are made using spring-loaded pressure contacts to the Au pads. Epoxy was the material of choice for the housing for two reasons: 1) to reduce the thermal mass and 2) to enable a hermetical sealing of the assembly to protect it from atmospheric humidity during the period prior to launch.

To ensure that the experiment can withstand the launch, we tested it under 50-g shocks along the three axes. In addition, the cryocooler with the device was operated inside a vacuum chamber while ejecting the heat into a thermal sink at 300 K. This temperature is close to what was designed to be the ambient temperature of the satellite in orbit. Following the integration of the experiment inside the satellite in May 1997, the whole satellite was further subjected to standard acceptance tests. The launch itself took place over a year later in July 1998.

In order to save power, we built a dedicated swept current source, which ramps the current through the device between zero and 100 mA over 3 s. The voltage across the device is read by a voltmeter every 10 ms. Once this voltage exceeds a preset value, the ramp is terminated and the time interval that has elapsed from the beginning of the ramp is recorded. The value of this time interval, in conjunction with the circuit parameters, allows us to calculate the resistance above T_c, and I_c below T_c. The current ramp is activated every 30 s during cool down. The experiment is terminated once I_c reaches 100 mA (a value of 100 mA corresponds to $J_c \approx 10^6$ A/cm^2) or if the total time allocated for the experiment has elapsed. All the parameters relevant to the operation of the experiment are programmable via telemetry from the ground station. The experiment is performed off line, and the recorded data is later transmitted to the ground station while the satellite passes overhead. For each initiation of the ramp, the data returned from the experiment includes the total time elapsed since the cooler and the experiment were turned on, the temperature, and the duration of the current ramp.

III. Performance In Orbit

In Fig. 2, we show the values T_c determined in orbit as a function of time since the launch. The time dependence of the critical current is shown in Fig. 3, in which we plot $T^\star$, the temperature at which I_c of the device reaches 100 mA. Comparing with the values measured at the time the device was prepared, some deterioration has evidently occurred during the year-long storage before launch. Several factors may have been responsible, but we feel that the most likely reason was humidity, resulting from an imperfect sealing of the device from the atmosphere. Additionally, there is a decrease in both quantities by about 2 K between the values recorded during the first run in orbit and the ones that follow. After that, the value of T_c recorded in orbit seems to decrease very slowly, by about 0.5 K/year. On the other hand, $T^\star$ remains constant within the scatter. Since any future devices will be operated at a temperature close to $T^\star$, i.e., well below T_c, these data imply that although some deterioration is seen, the time it will take to affect the properties of the device at the operating temperature will be significantly longer. We point out that our device is exposed to repeated thermal cycling. This is a more stringent mode of test than required of a device operating continuously at a fixed temperature. Thermal stress can induce microcracks in the film, especially when the films are thick.

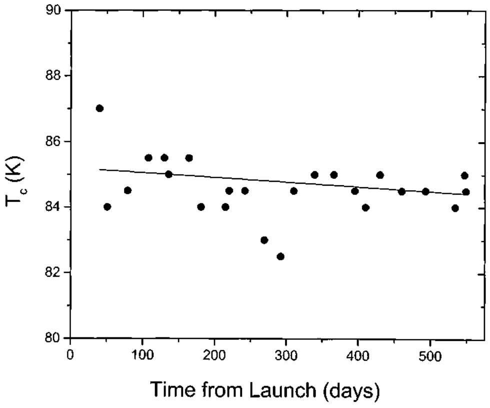

Fig. 2. Dependence of T_c of the film on time since launch. The solid line is a linear fit to the data.

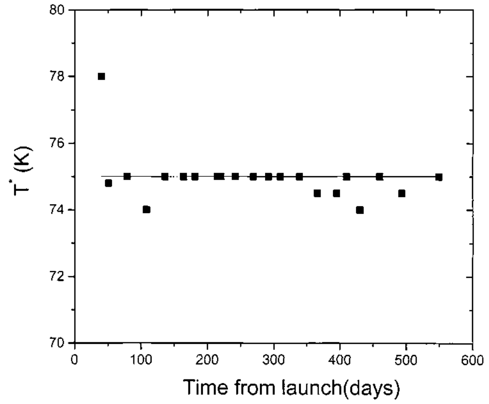

Fig. 3. Dependence of $T^\star$, the temperature at which I_c reaches 100 mA, on the time since launch.

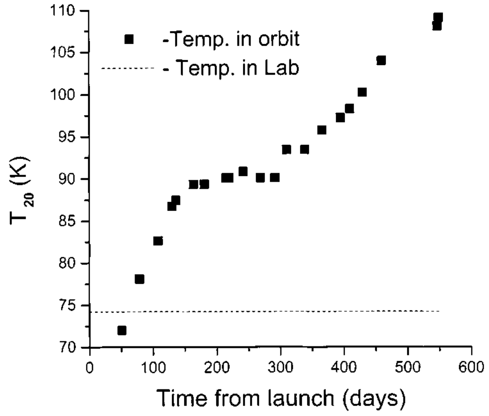

Fig. 4. Temperature reached by the experiment after 20 min of cooler operation, plotted versus time in orbit. The dashed line refers to the value measured during terrestrial testing.

This effect is well known with HTS films on buffered Si and, to a lesser degree, on sapphire. We, therefore, expect that the deterioration rate of systems, which operate continuously, will be lower than the one we are seeing.

Let us turn now to the behavior of the cryocooler. In Fig. 4, we show T_{20}, the temperature of the experiment recorded during each run after 20 min of operation. This temperature shows a systematic increase with time. This can result from either a continuous decrease of the cooling power of the cryocooler, from a deteriorating thermal contact between the thermometer-film Al block and the cold finger, or both. The fact that these data show some structure implies that there may be more than one factor involved. One hint comes from the differences of T_c and I_c recorded between the first and all subsequent runs in orbit. The relatively significant decrease between the first and subsequent runs can be the result of a release of the stresses accumulated during launch. It is plausible that the thermal contact between the thermometer and cryocooler has deteriorated for the same reason. On the other hand, progressively slower cool-down rate can also result from continuous loss of working gas due to a leak in the cooler. It can also result from a degradation of the contact between the cooler and its thermal sink on the cold panel of the satellite. We feel that worsening thermal contact of the thermometer block should be self limiting since even if the silver loaded glue cracks, there is still a pressure contact exerted due to the force of the 0–80-in bolts holding the assembly together. Since we see that T_{20} keeps climbing, there must be a real problem with the cooler as well. It appears, therefore, that the lifetime of our experiment will be eventually determined by the lifetime of the cryocooler.

IV. CONCLUSION

In summary, we have presented data on the material properties of YBCO thin films in space. Our data show a gradual decrease of T_c by about 0.5 K/year, measured under rather stringent test conditions of repeated thermal cycling. However, the critical current at the working temperature seems constant within our resolution, which is very promising. The ultimate lifetime of the experiment appears to be determined by the cooler.

ACKNOWLEDGMENT

The authors thank G. Shaviv, Physics Department, Technion—Israel Institute of Technology, Haifa, Israel, for including the superconductivity experiment in the TECHSAT package. The authors also acknowledge D. Cohen, Physics Department, Technion—Israel Institute of Technology, Haifa, Israel, E. Hadash, Physics Department, Technion—Israel Institute of Technology, Haifa, Israel, and A. Biran, RAFAEL, Haifa, Israel, for their contribution to this paper.

REFERENCES

[1] J. C. Ritter, M. Nisenoff, G. Price, and S. A. Wolf, “High temperature superconductivity space experiment (HTSSE),” *IEEE Trans. Magn.*, vol. 27, p. 2533, Mar. 1991.

[2] T. G. Kawecki, G. A. Golba, G. E. Price, V. S. Rose, and W. J. Meyers, “The high temperature superconductivity space experiment (HTSSE-II) design,” *IEEE Trans. Microwave Theory Tech.*, vol. 44, p. 1198, July 1996.

[3] E. Polturak, G. Koren, M. Ayalon, I. Flohr, R. Waller, and M. Guelman, “Design and performance of a space based high temperature superconductivity experiment,” *Appl. Phys. Lett.*, vol. 75, p. 1293, 1999.

[4] M. Guelman, I. Flohr, F. Ortenberg, M. Shachar, A. Shirayev, A. Volfovsky, and R. Waller, “The Israeli microsatellite Techsat for scientific research development and in-orbit testing,” *Acta Astronaut.*, vol. 46, no. 2–6, pp. 397–404, 2000.